JOURNAL OF AIRCRAFT
Vol. 47, No. 4, July–August 2010

Ionospheric Threat Parameterization for Local Area Global-Positioning-System-Based Aircraft Landing Systems

Seebany Datta-Barua*
San Jose State University, San Jose, California 95192
Jiyun Lee†
Korea Advanced Institute of Science and Technology, Daejeon 305-701, Republic of Korea
and
Sam Pullen,‡ Ming Luo,§ Alexandru Ene,¶ Di Qiu,¶ Godwin Zhang,** and Per Enge††
Stanford University, Stanford, California 94305

DOI: 10.2514/1.46719

Observations of extreme spatial rates of change of ionospheric electron content and the characterization strategy for mitigation applied by the U.S. local area augmentation system are shown. During extreme ionospheric activity, the gradient suffered by a global navigation satellite system user a few kilometers away from a ground reference station may reach as high as 425 mm of delay (at the GPS L1 frequency) per km of user separation. The method of data analysis that produced these results is described, and a threat space that parameterizes these possible threats to user integrity is defined. Certain configurations of user, reference station, global navigation satellite system satellite, and ionospheric storm-enhanced density may inhibit detection of the anomalous ionosphere by the reference station.

Nomenclature

B	=	satellite clock bias, m
b	=	receiver clock bias, m
D	=	ionospheric threat model maximum ionospheric delay, m
f_1	=	1575.42 MHz, GPS L1 frequency
f_2	=	1227.60 MHz, GPS L2 frequency
g	=	spatial rate of change of ionospheric delay, also known as *slope* or *gradient*, mm/km
I	=	slant ionospheric delay along signal ray-path at a given frequency (in this paper, L1), m
K	=	40.3 $m^3 s^{-2}$
N	=	integer ambiguity in number of cycles in carrier-phase measurement, dimensionless
N_e	=	electron number density, m^{-3}
r	=	true range between GPS satellite and receiver, m
rx	=	receiver location
sv	=	GPS satellite location
T	=	slant tropospheric error, m
t	=	time
v	=	ground speed of ionospheric storm or wave, front in the ionospheric threat model, m/s
w	=	ionospheric threat model spatial width of linearly varying region, km
$\mathbf{x}$	=	receiver position
ε	=	receiver noise and multipath, m
λ	=	GPS carrier signal wavelength, m
ρ	=	GPS pseudorange measurement, m
σ_{vig}	=	nominal standard deviation of ionospheric error broadcast to local area augmentation system users, mm/km
τ_{gd}	=	GPS satellite group delay, or interfrequency bias, m
ϕ	=	GPS carrier-phase measurement, m
i, j	=	subscript GPS receiver index
k	=	superscript GPS satellite index

Received 13 August 2009; revision received 29 April 2010; accepted for publication 29 April 2010.

*Assistant Professor, Department of Aviation and Technology, One Washington Square; Seebany.Datta-Barua@sjsu.edu.
†Assistant Professor, Department of Aerospace Engineering, 335 Gwahangno, Yuseong-gu (Corresponding Author).
‡Senior Research Engineer, Department of Aeronautics and Astronautics, Durand Building, Room 250.
§Research Engineer, Department of Aeronautics and Astronautics, Durand Building, Room 250.
¶Research Assistant, Department of Aeronautics and Astronautics, Durand Building, Room 250.
**Research and Development Engineer, Department of Aeronautics and Astronautics, Durand Building, Room 250.
††Professor, Department of Aeronautics and Astronautics, Durand Building, Room 250. Member AIAA.

I. Introduction

THE U.S. Federal Aviation Administration (FAA) is developing ground-based augmentation of the GPS, known as the local area augmentation system (LAAS), to provide differential GPS (DGPS) corrections to single-frequency users within tens of kilometers of a single airport [1]. The key element of this system is the LAAS ground facility (LGF), which is a DGPS reference station equipped with four GPS receivers (whose antennas are sited at known locations at the airport) and a vhf data broadcast link for sending corrections to users. A simple illustration of this configuration is shown in Fig. 1 (this figure will be addressed again in Sec. III to illustrate an ionospheric threat/user/LGF/satellite configuration). LAAS improves user accuracy by eliminating errors common to the user and reference stations and also provides a guaranteed level of integrity.

Integrity is an assurance provided to the user that bounds the difference between the unknown true position and the LAAS-derived position estimate with an extremely high degree of confidence. Anomalies or system failures that would violate this bound must be followed by a timely warning that either establishes a new bound or indicates that no guarantee can be made [2]. These bounds are computed by users in the position domain based on information broadcast by the LGF and are known as the lateral and vertical protection levels (VPL). Typically, the closer a maneuver brings an aircraft to a runway (i.e., the ground), the more stringent the requirements on integrity become. In particular, for aircraft approach and landing procedures, the vertical alert limits that the VPL must fall within are more stringent due to the presence of nearby obstacles.

The current version of LAAS is designed to meet the demands in accuracy, availability, and integrity needed for category 1 precision approaches. To do this, the system monitors many known error

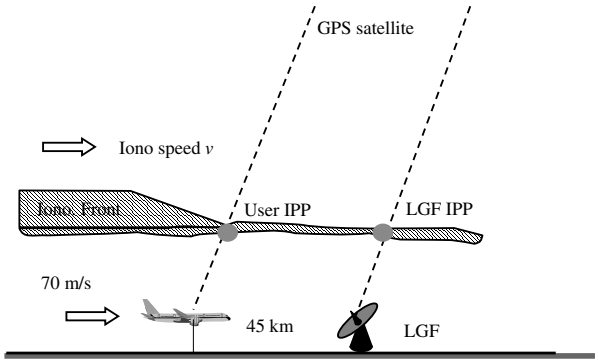

Fig. 1 Illustration of ionosphere-induced error for a LAAS user.

sources, including satellite ephemeris, clock, ionosphere, and troposphere, and also estimates bounds on the uncertainty of these error sources.

The GPS code and carrier-phase observables for the L1 signal frequency ($f_1 = 1575.42$ MHz) are [3]

$$\begin{aligned}\rho_1 &= r_i^k + b_i - B^k + T_i^k + I_i^k + \varepsilon_{\rho_1}\\ \phi_1 &= r_i^k + b_i - B^k + T_i^k - I_i^k + \lambda_1 N_1 + \varepsilon_{\phi_1}\end{aligned} \tag{1}$$

The true range r between the ith receiver and kth satellite, receiver clock bias b, satellite clock bias B, and tropospheric error T are nondispersive; they do not vary with signal frequency. The carrier phase contains an ambiguous integer number N of cycles of wavelength λ of the carrier frequency f_1 but has lower noise than the code measurement (i.e., $\varepsilon_\varphi \ll \varepsilon_\rho$). The ionospheric error I is frequency-dependent and, to first order, is of equal magnitude but opposite sign on the carrier phase relative to the code phase.

Of the various GPS error sources, error due to ionospheric delay is one of the largest and most variable for single-frequency GPS users. The ionosphere is a region of the upper atmosphere of Earth from about 50–2000 km in altitude that is ionized primarily by solar ultraviolet radiation [4]. Because of the free electrons and ions in this region, electromagnetic signals (such as those broadcast by GPS satellites) are refracted as they traverse the ionosphere. The main effect of this refraction is a delay in signal arrival time with respect to an identical signal traveling through free space. The cumulative delay is proportional to the total electron content (TEC), which is the density of electrons integrated along the signal path. The resulting ionospheric delay at L1 frequency, I (in meters), can be expressed as

$$I = \frac{K}{f_1^2}\int_{sv}^{rx} N_e \, dl = \frac{K}{f_1^2}\text{TEC} \tag{2}$$

where $K = 40.3$ m^3 s^{-2}, f_1 is the carrier frequency of the signal (Hz) and the integral is of the electron density, N_e (in electrons/m^3), over the path length of the signal from satellite sv to receiver rx [5]. Under ordinary or quiet ionospheric conditions, the ionosphere delays L1-frequency pseudorange measurements by one to several meters and advances L1 carrier-phase measurements by an equal amount. Ionospheric activity varies with location on Earth, time of day, season, and phase within an 11-year cycle of solar activity.

Under active ionospheric conditions, such as local daytime during the peak of the solar cycle, midlatitude ionospheric delays can reach 30 m or more at zenith and 2–3 times that for a low-elevation raypath, which passes through more of the ionosphere. More importantly for LAAS, the existence of large TEC values makes it possible for the ionosphere to have low spatial correlation. In such a case the ionospheric error suffered by the user may be very different from the error suffered at the ground station.

Figure 2 illustrates this potential magnitude and variability with a map of ionospheric delay over the eastern United States in the local afternoon during a magnetic storm at 20:15 universal time (UT) on 20 Nov. 2003. Color contours correspond to the meters of ranging delay error at the GPS L1 frequency from 0 (blue) to 20 m (red). The

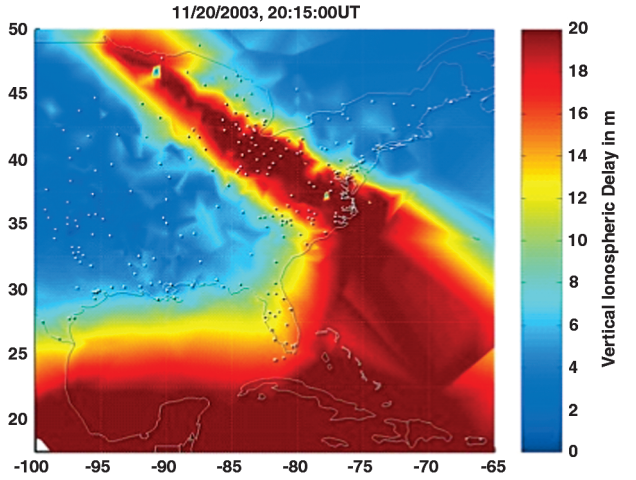

Fig. 2 Map of equivalent vertical ionospheric delay over eastern United States on 20 Nov. 2003 at 20:15 UT.

processing used to generate such a map is detailed in [6]. In short, this map is based on slant delays I measured from a network of GPS receivers (see Sec. IV on Data) viewing multiple satellites at different elevations. The point at which a line of sight (LOS) between a receiver and satellite reaches 350 km altitude is the ionospheric pierce point (IPP), which can be treated as an approximate location of the TEC producing that delay measurement. Multiple measurements are combined onto one plot via a geometric mapping function that converts elevation-dependent slant delays to equivalent vertical, or zenith, delays. From Fig. 2, it can be seen that equivalent zenith delays can vary by tens of meters over a couple of degrees of latitude and longitude during severe ionospheric disturbances.

A number of regional and global models of the electron density have been developed within the scientific community. In addition to entirely physics-based models [7–9] and empirical models (based on fitting parameters to historical data [10]), more recently, data-assimilative techniques that update a model based on measurements made over time have advanced [11–13]. However, these do not yet capture the structure and variability of the ionosphere during stormy periods like the one shown in Fig. 2, during which a storm-enhanced density (SED) with a poleward plume of ionization was observed over the conterminous United States (CONUS). Thus, these models cannot bound the impacts of ionospheric anomalies on the ionospheric error I of an aviation user with the high confidence levels required for integrity.

The LAAS LGF and aircraft, separated by some distance on the order of kilometers and viewing the same satellite, each suffer spatially correlated ionospheric delays. These simultaneous delay values will differ slightly because the LOS of the LGF and the LOS of the aircraft each pass through slightly different regions of the ionosphere. Theoretically, in the limit as the LGF and airborne receiver separation approaches zero, this difference in ionospheric delay vanishes.

Early work in addressing the feasibility of GPS augmentation systems in the presence of the ionosphere was done by Klobuchar et al. [14]. The correlation of ionospheric delays was estimated to be high enough that correction estimates could be made within a few hundred kilometers of the user's LOS [15]. This principle allows LAAS and the FAA's operational Wide Area Augmentation System (WAAS) to work in practice (note that WAAS, unlike LAAS, must guarantee the integrity of ionospheric corrections over baselines of hundreds of kilometers [16]).

For LAAS, Christie et al. [17] worked to quantify the ionospheric decorrelation rate for baselines of several kilometers. This paper estimated, based on data from several sites collected prior to 1999, that the differential delay at L1 would be from a few mm to, at most, 50 mm per kilometer of receiver separation. Because the ionosphere typically varies smoothly for a user and LGF who are usually separated by only a few kilometers, the nominal ionospheric error sigma broadcast to users (known as σ_{vig} [18]) is only a few mm of

delay difference per km of user-LGF separation distance [19]. The LAAS integrity bound calculation includes this term, and the need for a model to quantify anomalous behavior that might escape detection was not thought to be needed for baselines of less than 50 km.

However, Datta-Barua et al. [20] first investigated dual-frequency GPS network data during an ionospheric storm in 2000 that demonstrated that the differential delay could possibly be hundreds of mm/km. Luo et al. [21] posited a model for the user-LGF-ionospheric threat scenario and demonstrated that differential delays of hundreds of mm at L1 frequency per km could pose unacceptably hazardous conditions to a LAAS user under certain geometries and relative aircraft motions. The observation and impact of such high spatial rates of change in delay over short baselines invalidated the previous belief that the broadcast σ_{vig} would bound anomalous ionosphere. Since bounding was not possible, an ionospheric spatial-gradient threat model for LAAS, representing possible anomalies that could not be bounded by σ_{vig}, needed to be developed and mitigated to the degree that it threatened LAAS users. Developing this model took several years, involved several researchers, and required several iterations before culminating in the work presented here.

In this paper, we review the methodology of this data analysis and explain the current ionospheric threat model for CONUS, which must be mitigated by the LGF to meet the integrity requirements for CAT I precision approaches [22,23]. Sec. II provides the motivation for modeling anomalous ionospheric behavior, namely, the discovery that the differential error over baselines of a few kilometers can be hundreds of mm/km at L1. In Sec. III we develop a model for these spatio-temporal variations and define the fundamental parameters that characterize this model. Sec. IV introduces the dual-frequency GPS data sets that are used in this work and describes the uses and relative strengths of each. The algorithm for automated analysis and procedures for manual verification are investigated in Sec. V, which is the most time-intensive part of our study. The finalized threat space of this model incorporating the extreme parameter values are summarized in Fig. 13 of Sec. VI. Sec. VII contains our concluding remarks.

II. Severe Ionospheric Gradients Discovered in CONUS

The discovery of spatial rates of change shown in this section that are more than 2 orders of magnitude higher than nominal decorrelation rates motivates the need for an ionospheric threat model because such gradients could never be bounded by a practical broadcast sigma value. Measurements of ionospheric delay, or TEC, can be made with dual-frequency ranging receivers, which take advantage of the dispersive nature of the ionosphere, as given by Eq. (2). For dual-frequency GPS receivers, the observables at the L1 frequency are given by Eq. (1), and the observables at the second frequency (in this paper, $f_2 = 1227.60$ MHz) are

$$\begin{aligned}\rho_2 &= r_i^k + b_i - B^k + T_i^k + \gamma(I_i^k + \mathrm{IFB}_i + \tau_{\mathrm{gd}}^k) + \varepsilon_{\rho_2}\\ \phi_2 &= r_i^k + b_i - B^k + T_i^k - \gamma(I_i^k - \mathrm{IFB}_i - \tau_{\mathrm{gd}}^k) + \lambda_2 N_2 + \varepsilon_{\phi_2}\\ \gamma &= \frac{f_1^2}{f_2^2}\end{aligned} \tag{3}$$

The range r, clock biases b and B, and tropospheric error T are identical to those in Eq. (1). Similar noise terms ε and integer ambiguities N exist at the L2 frequency. The ionospheric delay at the L2 frequency is proportional to the delay I at the L1 frequency by the squared frequency ratio γ. Additionally, receiver hardware interfrequency biases (IFB) and satellite, τ_{gd}, affect the estimate of delay.

The slant ionospheric delay at L1 can be computed from the GPS code and carrier observables at L1 and L2 frequencies, given in Eqs. (1) and (3), in three ways:

$$I_\rho = \frac{\rho_2 - \rho_1}{\gamma - 1} \qquad I_\phi = \frac{\phi_1 - \phi_2}{\gamma - 1} \qquad I_{\mathrm{CMC}} = \frac{\rho_1 - \phi_1}{2} \tag{4}$$

The code estimate I_ρ is noisy because $\varepsilon_\rho \gg \varepsilon_\phi$ but has no integer ambiguity. The carrier estimate I_ϕ is low-noise but contains integer ambiguities for both L1 and L2. The single-frequency carrier minus code (CMC), or code-carrier divergence, estimate I_{CMC} is robust to the fragility of L2 codeless and semicodeless tracking loops, but contains both the L1 integer ambiguity and noise. In the dual-frequency estimates I_ρ and I_ϕ, the receiver and satellite hardware biases (IFB and τ_{gd}) must be removed.

For this initial study, high-quality ionospheric data for the CONUS region from the FAA WAAS network were used. WAAS had 25 ground stations over the United States during the period under investigation. Each ground station has three L1–L2 dual-frequency receivers, allowing for a direct measurement of the ionospheric delay. The raw receiver carrier-phase data is leveled to the code-phase data in postprocessing to remove integer ambiguities N_1 and N_2. Satellite bias τ_{gd} and receiver interfrequency bias IFB must be estimated and

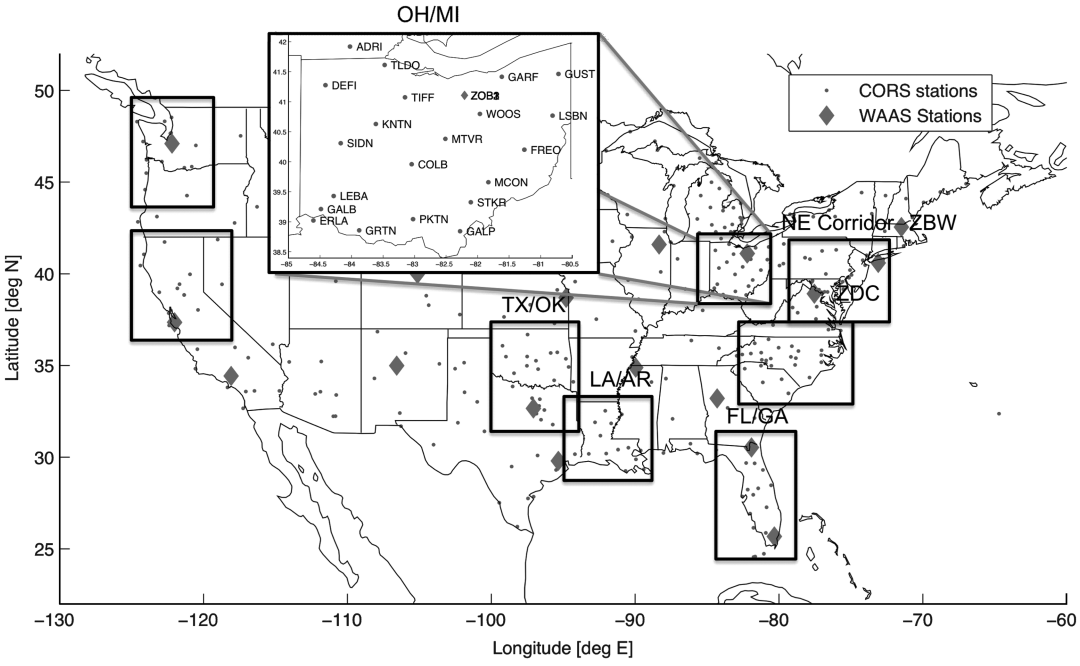

Fig. 3 Map of CORS station (dots) and WAAS reference station (diamonds) locations.

removed separately [24]. WAAS receiver redundancy allows for voting to remove possible artifacts due to problems on individual receivers. These data are reliable but geographically sparse relative to the LAAS service area, as the closest WAAS reference stations are 255 km apart. These locations are denoted with diamonds in Fig. 3.

To estimate the spatial rate of change possible in a LAAS configuration, the difference in delay along two lines of sight (LOSs), with a distance between them that is characteristic of LAAS, must be measured. One technique that is especially useful for analyzing differential delays when receivers are sparsely distributed is the time-step method, in which the IPP traversal distance over time substitutes for the LAAS ground station/aircraft separation [19].

WAAS data was used to identify times and regions exhibiting high rates of change as computed by the time-step method during the ionospheric storm of 6 April 2000 [20]. During this storm a large SED passed over CONUS, and its duskward edge caused high differential delays. Figure 4 shows the slant ionospheric delay in meters at each of the three WAAS receivers at ZDC as they track SVN 40. The horizontal axis below each subplot marks the elapsed time in seconds. For each receiver I_ρ (red), I_ϕ (blue), and I_{CMC} (green) are plotted. Both I_ϕ and I_{CMC} are recentered to the time-averaged code measurement of the delay I_ρ to account for the ambiguous integer number of cycles.

Over a time interval of 110 s, demarcated with vertical lines on Fig. 4, the receiver tracked through a drop in the slant ionospheric delay of about 8 m. There were no cycle slips (discontinuities in the measured ionospheric delay due to temporary receiver tracking problems) for any of the receivers during the time interval in question. The identical time evolution shown by all three receivers on all three forms of estimated delay indicates that the observed anomaly was not due to receiver bias.

A similar event for an independent LOS an hour and a half earlier on the same day further confirms the ZDC-SVN 40 anomaly. The receiver measurements of the ionosphere between the WAAS station ZBW and SVN 24 show that while station ZBW was tracking SVN 24 during a span of 150 s, the slant ionospheric delay on this LOS dropped by about 10 m. Given SVN 24's position in the sky during this time interval, the IPP of the ray-path traveled about 15 km. The fact that these observations represent two independent LOSs indicates that neither biases at an individual receiver or satellite nor cycle slips contributed to the high apparent decorrelation. Therefore, the anomalous events that affected LOS ZDC-SVN 40 and LOS ZBW-SVN 24 were both records of actual ionospheric events.

However, the gradients they imply (8 m at L1 over 7 km separation and 10 m over 15 km) may be artificially inflated for the following reason. The anomaly at station ZBW as it tracked SVN 24 preceded the anomaly along LOS ZDC-SVN 40 by 1.5 h. Ionospheric TEC maps for this storm period shown in the Appendix to [25] roughly indicate that the storm front whose boundary runs roughly east-west recedes southward for the duration. Having first been traversed by an IPP from station ZBW, it progresses south to be traversed by an IPP from ZDC 1.5 h later. Based on this observation, to first order, its velocity $v_{\mathrm{front}} = 110$ m/s southward. The IPP associated with ZDC-SVN 40 was moving primarily northward with ground speed, $v_{\mathrm{IPP}} = 7$ km/110 s $= 63$ m/s, respectively. The velocity of the storm front is nonnegligible compared with the IPP velocity. Since the velocities were directed roughly opposite to each other, the additive effect of the relative velocities would make the spatial gradient in the ionosphere appear to be a factor of two, or more, worse than it actually was. Instead of a 7 km width, the width w of the storm front was more likely

$$w = (v_{\mathrm{front}} - v_{\mathrm{IPP}}) \times t = (110 - (-63)) \times 110 = 19,030 \text{ m} \quad (5)$$

This means that the purely spatial gradient of the ionosphere was more likely 8 m of slant delay difference over a 19 km range, w, as shown in Eq. (5), giving a 420 mm/km spatial rate of change of slant delay.

From this event, we learned about the potential existence of spatial rates of change in ionospheric delay with magnitudes that could not be bounded by the LAAS nominal broadcast correction. We also observed that estimating the spatial rate of change is complicated by the mixing of spatial and temporal variations in the ionosphere through SED motion, as well as the motion of LOSs relative to the ionospheric structure.

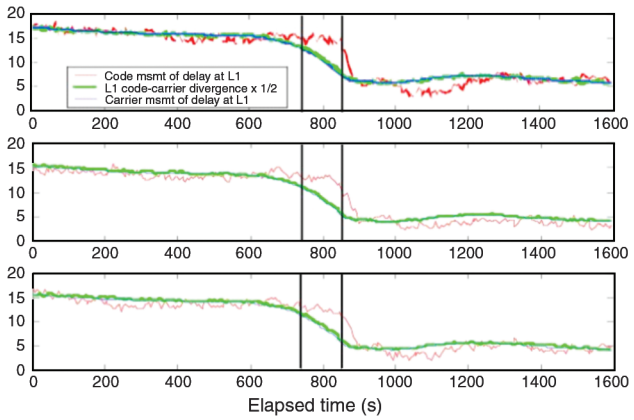

Fig. 4 Slant ionospheric delay, in m, between WAAS receivers at Washington, D.C., and GPS satellite 40 on 6 April 2000.

III. Ionospheric Threat Model Parameterization

The discovery of high spatial gradients at the edges of ionospheric SEDs, combined with relative motions of the ionosphere and LOSs, was used to develop an ionospheric threat model for identifying possible threats to LAAS users. In this section, we define a model for an ionospheric wave front and associated model parameters.

Based on the findings in Sec. II, the ionospheric threat is modeled as a spatially linear semi-infinite wave front with constant propagation speed. Figure 5 illustrates this model. The model is parameterized by the slope g of the ramp and its width w, the product of which yields a maximum ionospheric delay D, and the ground speed v of wave front. The observations in Fig. 4 of a constant high delay, a period of decline at a fairly constant rate, and a period of constant low delay supports the piecewise linear model. A higher order model may fit the actual data better. However, simplicity in the mathematical form of an ionospheric threat model enables easier assessment of impact on users through LAAS simulation tools and identification of mitigation strategies.

The maximum ionospheric delay difference is upper-bounded by a maximum value which was set based on observations. Slope and width values whose product creates a maximum delay difference above the bound on D are not part of the threat model and are discarded. This limit is conservative because it allows for possible ionospheric configurations that may be physically impossible, but it keeps the simulation search space tractable. In any case, as Luo et al. [26] showed, the extreme regions of the search space will be easily detected by the LGF within the time to alarm when the ionospheric front is very wide and thus sweeps across the field of view of the LGF. Fortunately, the impact of ionospheric wave fronts on LAAS is not very sensitive to width; thus the choice was made to include a range of possible front widths from 25 to 200 km in the threat model. Larger widths would not produce gradients sufficiently sharp to be threatening, and smaller widths would not cause much difference in LAAS impact simulation results [27]. Thus, data analysis procedures are devoted to estimating the slope g and speed v of ionospheric wave front (Sec. V).

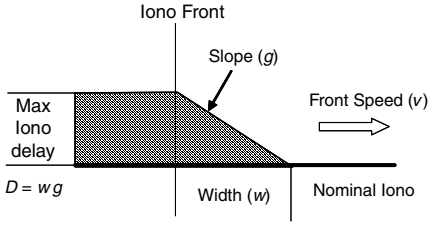

Fig. 5 Ionospheric wave-front model.

As noted above, the gradient is assumed to represent a linear change in slant ionospheric delay between maximum and minimum delays. As a result, the bounding slant gradients are also (at least potentially) functions of satellite elevation.

To recap, this threat model assumes severe ionospheric spatial gradients take the form of straight, horizontally semi-infinite wave fronts of linearly varying TEC that move at constant speed and direction with respect to the ground. In addition, the slope of the ramp itself is not time-varying. These are simplifications of reality but are reasonable for the duration of an aircraft approach. These assumptions are adequate because deviations from them do not materially change the final result, except if most-evil variations (compounding the worst-case upon the worst-case) are allowed.

The ionospheric threat model does not include other parameters that are necessary for simulating and assessing impact on LAAS-equipped aircraft, such as the orientation of the ionospheric wave front with respect to the aircraft and runway, the horizontal approach speed of the aircraft, the approach direction of the ionospheric front, the initial position of the ionospheric front with respect to the aircraft at the start of the simulation, and the velocities of the IPPs, which are driven by satellite and receiver motion. Figure 1 illustrates an example of one possible configuration of the ionospheric threat model/user/runway/satellite scenario.

IV. Data

The remaining sections of this paper are concerned with identifying the worst observed values of the ionospheric threat model parameters of slope and speed at different ranges of elevation angles. Existing ionospheric models do not capture anomalous behavior such as that observed on 6 April 2000, so our threat-space development for the ionosphere is data-driven. Precise estimates of ionospheric delays can be obtained using dual-frequency GPS measurements from networks of stations and sophisticated post-processing algorithms.

The U.S. National Geodetic Survey makes dual-frequency GPS data publicly available in RINEX format from a network of continuously operating reference stations (CORS) [28]. CORS has hundreds of stations in CONUS, (sites as of 29 Oct. 2003 are shown in Fig. 3), and permits ionospheric measurement comparisons across baselines of tens of kilometers. Before analysis, geographical clusters of the highest-density receiver regions in the United States are targeted to provide the best possible spatial resolution. Eight clusters over CONUS of around 21 square degrees of average area are defined and boxed in Fig. 3. Each of these clusters contains 10–30 receivers with baseline separations of 15–200 km. Most of the data analysis is performed for stations inside these clusters. In some cases additional stations adjacent to these clusters are also used to better capture ionospheric wave-front behavior that extended beyond cluster boundaries.

The dates from which data were collected and analyzed are shown in Table 1, along with the publicly available indices of global geomagnetic activity, planetary K (Kp) and *disturbance, storm time* (Dst), and geomagnetic storm class (G-class), and WAAS coverage. Particular geographic regions of focus, if applicable, are shown.

The values of Kp, Dst, G-class, and WAAS coverage are used to help target days on which anomalous behavior in CONUS was likely to have occurred. Because the ionosphere is coupled to the magnetosphere, which is in turn driven by the solar wind, measures of geomagnetic activity provide information about the ionosphere by proxy. The Dst index measures activity in the worldwide geomagnetic field [29,30], with negative deviations indicating ionospheric currents and activity. Kp is a three-hour composite index based on geomagnetic activity measured at several midlatitude stations primarily located in the northern hemisphere [31,32]. Kp ranges in thirds of an index unit from 0 (no activity) to 9 (extreme activity). The Space Weather Prediction Center of the National Oceanic and Atmospheric Administration has developed a geomagnetic storm scale and associated descriptors for use by both the technical community and the general public [33]. The scale varies from G1 through G5, and the storm classes associated with each level, in order of increasing intensity are: minor, moderate, strong, severe, and extreme.

The percentage of WAAS coverage indicates the degree to which these storms introduced nonlinear spatial variations over CONUS (viewed over separations of hundreds of km between WAAS reference stations), limiting WAAS availability for precision approach. While the other measures shown in Table 1 are global, WAAS coverage is a daily summary value that indicates how much impact each storm had in the American sector, where the CORS stations are sited. For the dates occurring before WAAS initial operating capability (IOC) official coverage percentages do not exist.

The data collected from the CORS network have been assimilated and had biases removed by the use of the global ionospheric mapping (GIM) software at NASA's Jet Propulsion Laboratory (JPL). With the additional use of the publicly available International GNSS Service station data worldwide, GIM estimates and removes satellite and receiver interfrequency biases to provide high-precision ionospheric measurements. The dual-frequency ionospheric observables, I_{DF}, are computed by leveling the phase estimates, I_ϕ, using the code estimates, I_ρ. The processing with a leveling function, f, is described in detail in [34]. The resulting data are provided at 30 s intervals:

$$I_{\mathrm{DF}} = f(I_\rho, I_\phi) \tag{6}$$

CORS ionospheric estimates are processed in a similar manner to those of WAAS (see Sec. II), but the lack of multiple receivers at each site means that anomalies due to receiver glitches cannot be voted out. In addition, the quality of CORS receiver equipage and siting is much more variable than that of WAAS reference stations; thus typical CORS receiver measurement errors are several times higher than that of WAAS receivers. The screening algorithms used at JPL are based on an error detection threshold that was set to allow more data points and minimize the risk of discarding true ionospheric events.

V. Data Analysis Procedure

The objective of this section is to produce the LAAS threat space on parameters g and v using the data from closely-spaced CORS stations described above. The procedure for processing CORS

Table 1 Ionospheric storm dates and conditions investigated

Day (UT mm/dd/yy)	Kp	Dst	Geomagnetic storm class	WAAS coverage	Focus region
04/06/00	8.3	−287	Severe	None (pre-IOC)	NE corridor
04/07/00	8.7	−288	Extreme	None (pre-IOC)	NE corridor
07/15/00	9.0	−289	Extreme	None (pre-IOC)	——
07/16/00	7.7	−301	Strong	None (pre-IOC)	——
09/07/02	7.3	−163	Strong	None (pre-IOC)	——
10/29/03	9.0	−345	Extreme	∼0%	——
10/30/03	9.0	−401	Extreme	∼0%	TX–OK–LA–AR
10/31/03	8.3	−320	Severe	∼0%	FL–GA
11/20/03	8.7	−472	Extreme	∼0%	OH–MI
07/17/04	6.0	−80	Moderate	∼68.8%	TX–OK–LA–AR

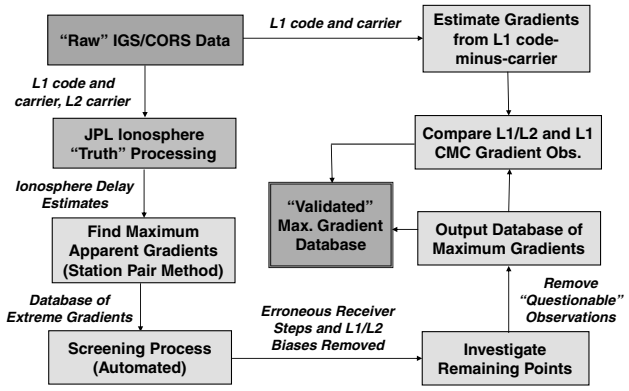

Fig. 6 Ionospheric anomaly data analysis procedure.

receiver data, identifying anomalously high spatial rates of change, validating anomalies that are due to ionospheric events, and estimating parameters in terms of the threat model of Sec. III is shown in Fig. 6. The starting point is raw L1 and L2 measurements from selected clusters of CORS stations. An automated algorithm, flowing down the left-hand side of the figure, involves using the JPL-processed CORS-based estimates of ionospheric delay to compute apparent spatial gradients and front speeds, and screen them for obvious receiver or data-processing errors. The remaining points are compared manually (right-hand side of Fig. 6) to estimates derived from raw CORS data. The following sections trace through the methodology outlined in the flowchart in Fig. 6.

A. Ionospheric Spatial-Gradient Estimation

1. *Station Pair Method*

Our approach involves considering selected pairs of CORS stations in the JPL-processed database as though they represent an LGF-user receiver pair (with a static user position). This technique, called the station pair method, is illustrated in Fig. 7. For each epoch t, the delays at each of two stations i and j viewing the same satellite k are differenced. The slope of ionospheric delay, ∇I, between all pairs of receivers looking at each satellite is estimated by dividing the differential slant delay by the baseline distance between the two receivers:

$$\nabla I(t) = \frac{|I_i^k(t) - I_j^k(t)|}{\|\mathbf{x}_i - \mathbf{x}_j\|} \tag{7}$$

The station pair method, unlike the time-step method (Sec. II), does not artificially inflate ionospheric gradients due to relative motions of IPPs and the ionosphere [19].

The dual-frequency data in each CORS cluster are separated into five elevation bins: 0–12, 12–20, 20–30, 30–45, and 45–90 deg. For each LOS elevation range, receivers in each cluster are grouped into pairs, and I_{DF} is used for I in Eq. (7), to give a dual-frequency estimate of the gradient ∇I_{DF}.

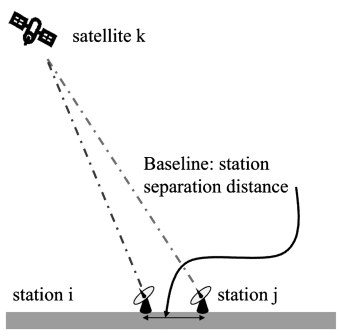

Fig. 7 Station pair method. Not to scale.

2. *Automated Screening*

After ∇I_{DF} is computed, an automated screening process (bottom-left corner of Fig. 6) isolates the most credible events above a chosen threshold (100 mm/km) and eliminates those gradients that are apparently due to nonionospheric causes. Cases for which two receivers are effectively collocated (less than 100 m apart) or the slant gradient ∇I_{DF} does not vary in time are attributed to an interreceiver bias and eliminated. Cases for which ionospheric delay measurements from one receiver do not vary in time are attributed to a faulty receiver and eliminated.

Variations greater than 15 mm/s ionospheric delay rate of change are flagged for possible ionospheric activity. The 15 mm/s threshold is set to be an order of magnitude lower than the largest time rate of change observed for the 29 Oct. 2003 storm day [35], in order to allow significant rapid changes in the delay value to pass screening as possible ionospheric events. The advantage of this threshold is that real ionospheric events are less likely to be eliminated as false negatives. The tradeoff is that false alarms occur when the data contain cycle slips, causing the delay value to jump suddenly between two successive measurement points. These cases have to be eliminated manually from the screening results.

3. *Manual Validation*

The plausible ionospheric events that survive the computer-automated screening process are analyzed manually. For each of these events, visual analysis determines whether the magnitude of the gradients, together with the length of time that these gradients manifest themselves look reasonable or are more likely to be artifacts of faulty receiver tracking.

The first step in verifying an event is by comparison against simultaneous observations of slant delay from other nearby receivers in the same cluster. This can be thought of as cluster-wide voting that operates in a similar manner to the voting among colocated receivers at each WAAS reference station. If other nearby CORS receivers exhibit similar ionospheric delay patterns to the pair that shows the most-extreme spatial decorrelation, the event is very probably real and is not limited to a single receiver fault. On the other hand, if the observations were influenced by receiver artifacts in the data, it is unlikely that a majority of the receivers in the cluster contain the same or similar artifacts.

To support this comparison, plots are constructed that extend across the entire period of time for which data was extracted so that the receiver behavior can be analyzed both in the presence of disturbed ionosphere and also during calm ionospheric conditions on either side of the disturbance. While the electron content within the ionosphere is expected to vary wildly during the actual storm, delay measurements from the different receivers within a CORS cluster are expected to converge to similar values at times of nominal ionospheric activity. Quiet periods of ionospheric behavior help to establish a baseline for the affected receiver cluster and give an indication of any possible interreceiver biases.

The next step in validating extreme gradients, (top-right corner of Fig. 6), is to estimate approximate wave-front parameters from raw L1 code-minus-carrier measurements I_{CMC} and compare them to the observations from the JPL-processed dual-frequency data I_{DF}. The L1-only estimates of these slopes ∇I_{CMC}, given by using I_{CMC} for the slant delay I in Eq. (7), provide a picture of gradients that is not subject to fragile L2 tracking loops. The L1-only estimates are not exact, however, because the integer ambiguity N_1 has not been eliminated.

Two methods are used to remove the integer ambiguity for high-elevation and low-elevation LOSs, respectively. For high elevation, the postprocessed L1/L2 estimate of absolute differential slope ∇I_{DF} at a time well before or after the wave front passes is used to initialize the single-frequency ionospheric gradient estimates ∇I_{CMC}. A point in time is picked at which the measurements ∇I_{CMC} are aligned to ∇I_{DF} by subtracting a constant bias from all the measurement of one of the receivers, equalizing the value that they measure at the chosen instant. Since the differential delay between a pair of receivers is observed, this is equivalent to choosing a reference zero-slope point

in ∇I_{CMC} at a particular instant in time and then expressing all other slope measurements relative to it. Thus, L1 CMC ionospheric gradient estimates form lower bounds on the true gradient, but these estimates are accurate enough that they can be used to validate the L1/L2 observations.

For low-elevation satellites, the track may not be long enough to sample through quiet ionosphere. In this case, the single-frequency gradient estimate is leveled to the mean of the JPL-processed dual-frequency estimate, ∇I_{DF}, as shown in Eq. (8):

$$\nabla \tilde{I}_{\mathrm{CMC}}(t) = \nabla I_{\mathrm{CMC}}(t) - \overline{\nabla I_{\mathrm{CMC}}} + \overline{\nabla I_{\mathrm{DF}}} \tag{8}$$

Anomalous ionospheric events not eliminated by this final manual comparison to single-frequency estimates $\nabla \tilde{I}_{\mathrm{CMC}}$ of the spatial variation are deemed to be validated measurements, $\nabla I_{\mathrm{DF_{Validated}}}$, and are used to generate bounds on the threat model parameter g:

$$g = \max_{t}(\nabla I_{\mathrm{DF_{Validated}}}) \tag{9}$$

B. Ionospheric Front Speed Estimation

Observations of severe gradients that are validated as described in Sec. V.A are studied in more detail to characterize them in the context of the ionospheric threat model geometry. The automated code used a three-station-based trigonometric algorithm to estimate the speed and direction of wave-front propagation with respect to the ground (see [22] for details). The travel time of the front which swept a pair of stations is measured to compute the speed, and the third station is used to observe the front direction. This algorithm proved to be very sensitive to measurement errors and limitations of the threat model (in particular the assumption that the wave front is a straight line) when extrapolated to cover three (instead of two) stations.

To overcome the weakness of the automated ionospheric front speed computation method, a manual two-station-based method is used that takes wave-front orientation (estimated manually based on many stations) as an input so that only speed needs to be solved for. First, we form groups that typically include four to eight nearby CORS receivers which show similar ionospheric delay patterns to the satellite-receiver pair from which anomalous gradients were observed and verified. By observing the time history of ionospheric slant delays from the stations observing the same satellite, the peak delay times, t_{peak_i}, at which the slant delay of the station i reached the local maximum value are determined. Because ionospheric delays of these nearby stations exhibit similar patterns, the order in which the stations were affected by the ionospheric front can be deduced from t_{peak_i}. This order and the locations of the affected stations make it possible to approximately determine the forward propagation direction of the front. Since it was assumed that the wave front is a straight line and moves with constant speed, which is not true in reality, the sequence and t_{peak_i} must be carefully adjusted manually. Also, the slant delays sometimes appear to have more than one local maximum, and this ambiguity makes room for t_{peak_i} to be fine-tuned considering the underlying assumptions.

Next, we select a pair of stations (i, j) and determine the travel time $\Delta t_{i,j}$, given by Eq. (10):

$$\Delta t_{i,j(i\neq j)} = t_{\mathrm{peak}_i} - t_{\mathrm{peak}_j}; \qquad i, j = 1, 2, \ldots, N \tag{10}$$

The distance between the two stations projected onto the line perpendicular to the wave front,d_n, is used to compute the speed of the wave front, v_n, as shown in Eq. (11):

$$v_n = \frac{d_n}{\Delta t_{i,j(i\neq j)}} \tag{11}$$

Note that this speed estimate contains the velocity component resulting from the movement of the satellite in addition to that from actual wave-front motion. Thus, the (notional) IPP velocity is computed and removed so that the resulting wave-front velocity estimates are referenced to a fixed point on the ground (such as an LGF site). IPP velocity and direction are computed from the CORS data, which give the notional IPP locations for each satellite at 30 s intervals. The purpose of using IPP velocity, even though the IPP concept is not otherwise used in defining this threat model, is to capture in an average sense the speed of the ray-path motion through the ionosphere. We repeat this computation for all combinations of stations and obtain a range of front-speed estimates that are normal to the ionospheric front. Finally, we take the mean value of the resulting speed estimates, which is the manually estimated and validated wave-front velocity with respect to the ground.

VI. Results: CONUS Ionospheric Anomaly Threat Model

In this section we analyze two case studies following the process described in Sec. V. These two cases are of particular interest because they give the maximum dual-frequency verified slopes we observed at high elevation (Sec. VI.A) and at low elevation (Sec. VI.B), respectively. Both cases were observed from the Ohio/Michigan cluster shown in the inset of Fig. 3 and show very weak elevation dependence. We then summarize the resulting threat model for CONUS.

A. Case Study 1: High Elevation

Figure 8 shows the slant ionospheric delay from this event as observed by seven CORS reference stations in northern Ohio and southern Michigan as they tracked GPS SVN 38. Note the rapid growth in delay associated with the passage of the leading edge of the plume of enhanced delay shown in Fig. 2 in just under an hour, followed by an interval of erratic variation in ionospheric delay within the plume while the overall delay remains high, followed by a sudden, steep drop-off corresponding to the duskward edge of the plume. The JPL-processed dual-frequency delays (Fig. 9a) and elevation angles (Fig. 9c) over time are shown for ZOB1 (red) and GARF (green), which are separated by only 51.2 km. The dual-frequency estimate of the slope ∇I_{DF} between these stations is shown in Fig. 9b.

Data outages on both ZOB1's and GARF's dual-frequency measurements are visible in Fig. 9a. The drop from 30 to 18 m on the GARF (green) curve at 2055 UT and on ZOB1 (red) at 2100 UT calls into question the reliability of the dual-frequency estimate of the slope. For this reason, we validate the presence of an actual ionospheric spatial anomaly within this data by comparing ∇I_{DF} (blue) with the single-frequency estimate of the slope ∇I_{CMC} (red) in Fig. 10. The data outages present from 2055 to 2100 UT in ∇I_{DF} do not exist in the L1-only measurements, confirming that the data gaps are limited to L2 measurements. The general trend over time between the two slope measurements agrees, including the time during which L2 data outages occur. Based on the similarity of this event to observations (Fig. 8) by other receivers in the vicinity, we can

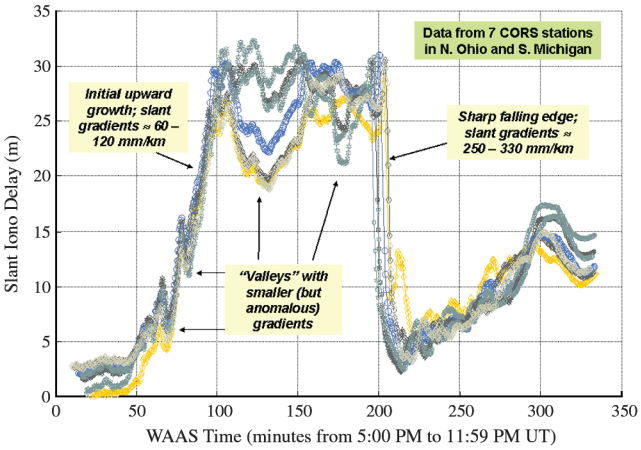

Fig. 8 Dual-frequency estimates of slant ionospheric delay from JPL-processed CORS data vs UT hour for select stations in the Ohio/Michigan cluster tracking SVN 38 at high elevation.

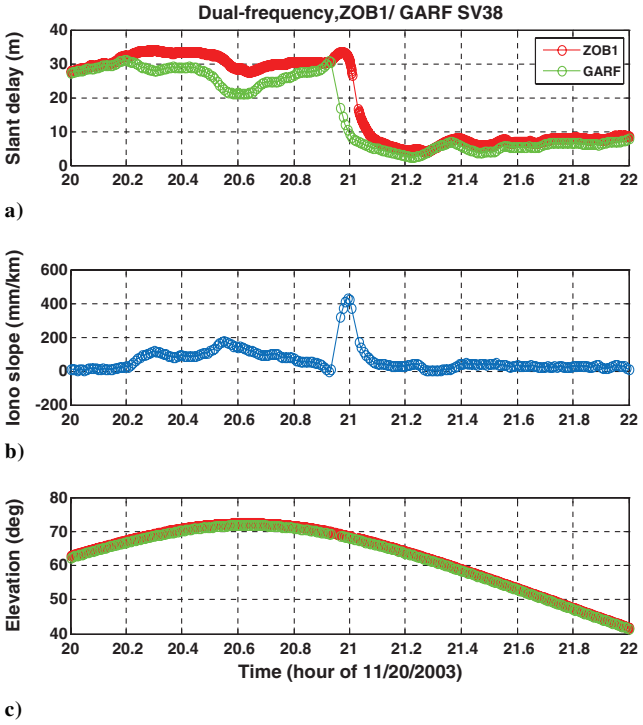

Fig. 9 Maximum ionospheric gradient observed at high elevation: a) dual-frequency estimates of slant ionospheric delay, b) spatial rate of change, and c) elevation from JPL-processed CORS data vs UT hour for receivers ZOB1 and GARF tracking SVN 38 at high elevation.

confirm a maximum slope observed due to this event of 413 mm/km at 2100 UT.

B. Case Study 2: Low Elevation

We also investigate data to show the largest-magnitude ionospheric gradients that we have validated at low elevation (less than 15 deg) at 2130 UT. Figure 11 is a plot of the dual-frequency measurements of slant ionospheric delay over time at these stations when observing SVN 26 to the northwest at about 12 deg elevation (not shown). The two stations FREO and WOOS (see inset of Fig. 3 for location) begin at 15 m and rise to over 45 m of slant delay as the

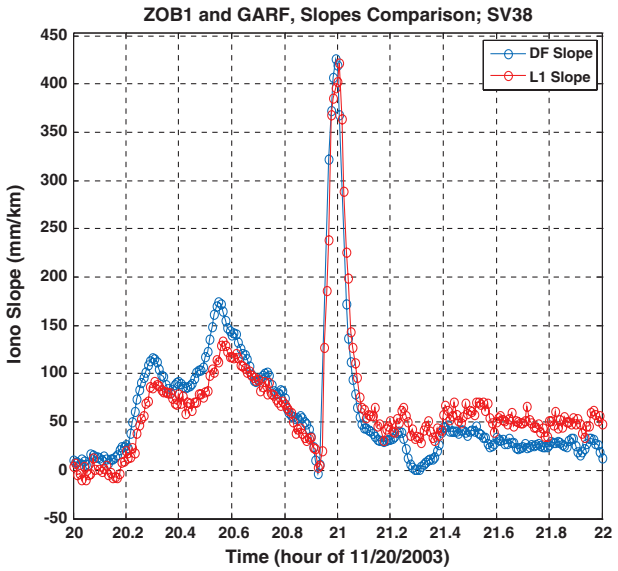

Fig. 10 Spatial rate of change of ionospheric delay over time between two stations in Ohio/Michigan cluster viewing SVN 38 at high elevation, from ∇I_{DF} (blue) and ∇I_{CMC} (red).

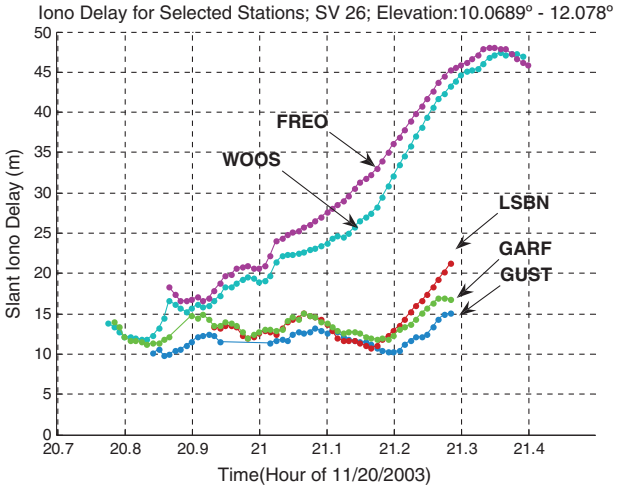

Fig. 11 Dual-frequency estimates of slant ionospheric delay from JPL-processed CORS data vs UT hour for select stations in the Ohio/Michigan cluster tracking SVN 26 at low elevation.

LOSs from these stations to SVN 26 pass through the filament of enhanced ionospheric delay.

We analyze the WOOS–GARF pair of stations to estimate the ionospheric spatial gradient between them. The dual-frequency-based slope ∇I_{DF} is plotted in blue on Fig. 12. The slope rises from 0 mm/km to nearly 400 mm/km as the delay for WOOS rises to 45 m during passage through the anomalous region, while GARF holds steady at about 15–18 m. There is a dual-frequency data gap for GARF at 2054 UT that contributes to the data gap in ∇I_{DF}; however, the outage is not simultaneous with the highest slope observed between this station pair.

The dual-frequency estimate is compared with the single-frequency estimate of the ionospheric spatial gradient, ∇I_{CMC} (green on Fig. 12). Continuous single-frequency measurements exist except at one epoch at 2052 UT, at which time the L1 measurements had a visible cycle slip that was manually removed. Based on the agreement between the two measurements, we conclude that the highest slope between the stations WOOS and GARF occurs at 2120 UT and is about 360 mm/km.

C. LAAS Ionospheric Threat Space

Using the method described in Sec. V and illustrated in the subsections above, numerous other instances of high differential delay between receivers closer than 100 km were investigated from multiple storm days in CONUS listed in Table 1. This was a multistage, multiperson process spanning data from storms from

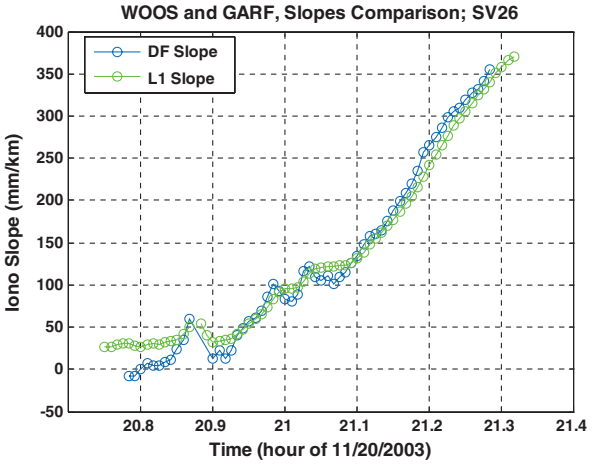

Fig. 12 Spatial rate of change of ionospheric delay over time between two stations in Ohio/Michigan cluster viewing SVN 26 at low elevation, as from ∇I_{DF} (blue) and ∇I_{CMC} (green).

2000–2005, during the maximum and waning phases of the most recent solar cycle.

Figure 13 summarizes the results of this data analysis process by populating the threat space with cases observed in CORS data from the storms examined. In Fig. 13a, the instances of anomalous gradients are plotted as a function of slope (mm/km) on the horizontal axis and ground speed (m/s) on the vertical axis. The points that were identified in dual-frequency data and subsequently verified with single-frequency L1 code-minus-carrier data are marked with diamonds. The points that were estimated from the ∇I_{CMC} directly are shown as triangles. These same points are plotted in Fig. 13b as a function of elevation angle (degrees) on the horizontal axis and slope (mm/km) on the vertical axis.

Note that width estimates do not appear in this figure. The width of the TEC ramp was generally difficult to assess from the available data given the typical 50–100 km separation of CORS reference stations. In addition the integrity results (i,e,, the threat model impacts on LAAS users) were not found to be sensitive to this parameter [27].

Empirical bounds are fitted to the points shown in Fig. 13, in order to limit the threat space to the maximum gradients discovered and validated. These bounds are marked with solid lines in Fig. 13. Figure 13a shows that for events moving at speeds less than 90 m/s with respect to the ground, a maximum slope of 150 mm/km bounds the events observed. Figure 13b shows the upper bound on the maximum gradient of this threat model as a function of satellite elevation angle for speeds greater than 90 m/s: a slope of 375 mm/km at low elevation, increasing linearly at a rate of 1 mm/km from 15 to 65 deg elevation, to reach 425 mm/km at high elevation. For ground speeds below 90 m/s, the maximum slope is 150 mm/km, independent of elevation. These bounds slightly exceed the largest gradients validated from the data analysis due to margin added to account for measurement error. In addition to the plotted maximum gradient and speed bounds, width (distance between high and low delay regions) is delimited to be between 25 and 200 km, and total slant differential delay up to 50 m [22,36].

Figure 13a shows a maximum estimated ionospheric front speed of about 600 m/s with respect to the ground, and the speed was limited to be no more than 750 m/s. This bound is based on a number of considerations. First, in practice the absolute speed is of secondary importance to the front speed with respect to the aircraft and LGF ray-paths (or effectively, their IPPs). The relative motion permits detectability; in fact the estimates of speed were very sensitive to this relative motion. There is a real (albeit unlikely) possibility that IPP speed might cancel out the actual ionospheric front speed relative to the ground and thus prevent time-based LGF monitoring from detecting very large gradients for several minutes. This possibility significantly increases the maximum possible ionosphere-induced error for LAAS users beyond what was initially projected in work that did not consider this masking possibility (e.g., [37]). It also affects the ionospheric anomaly simulation algorithms described in [23,38], as the method for selecting the worst possible ionospheric front from the point of view of a given satellite is now dictated by the theoretical speed of the resulting IPP.

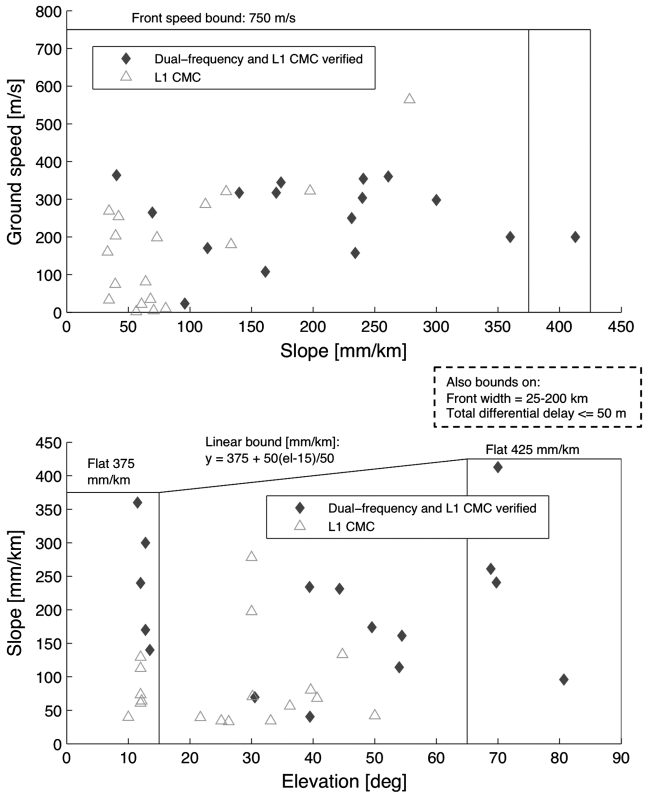

Fig. 13 Ionospheric gradient threat space: anomalous ionospheric gradients observed plotted in threat model space as a function of a) slope and ground speed and b) elevation and slope.

The threat space shown in Fig. 13 is used to represent what the ionosphere is potentially capable of during rare extreme-ionospheric-storm conditions based on the validated events observed in the ionospheric data analysis described in Sec. V. However, in adopting this threat model for the present, we must recognize that the validated events that have occurred to date are few in number, since they are driven by the most extreme storms that have impacted the American sector and cover a limited geographical area within CONUS due to constraints imposed by the CORS receiver sites and equipage. It is possible that localized events severe enough to potentially threaten LAAS users have occurred in CONUS but are not included in the data used to construct the threat space. Therefore, while this threat space is deemed final for the purposes of CAT I LAAS certification [39], the anomaly mitigation algorithms have adjustable parameters in case future ionospheric storms or data analyses reveal gradients that fall outside this threat space. Another possibility is that better understanding of how the ionosphere behaves during storm events will allow us to reduce the conservatism in the model as well as develop a more physically accurate description of how ionospheric anomalies propagate through LGF and user observations.

Users can be protected from these situations by inflating the protection bound that is broadcast to exclude geometries that would lead to intolerably large positioning errors [23,38]. Even though there is no evidence of such large gradients on nominal days, without the ability to detect ionospheric storms in real time that is possessed by WAAS, LAAS must assume that the ionosphere may be in a disturbed state at all times. As a result, geometries that would be unsafe during a storm are disallowed even though severe storms are very unlikely to be present; thus sacrificing precision approach availability. One method for excluding geometries that achieves an acceptable level of availability is described in [23].

VII. Conclusions

This paper represents the culmination of several years of teamwork in conducting as comprehensive a search as possible for past extreme ionospheric events in CONUS that would impact LAAS user safety. We have identified the ionospheric threat to users of LAAS, parameterized a model to represent it, and applied a two-phase method of ionospheric spatial-gradient analysis and validation to quantify the magnitude of these threats. This method consists of automatic processing of dual-frequency GPS carrier-phase measurements of ionospheric delay combined with manual comparison to single-frequency code-carrier divergence measurements to search for an upper bound on possible anomalous ionospheric gradients. The final threat space of the model is ultimately driven by the largest of these points found, but the parameters of this model have gone through a number of revisions in magnitude throughout this process. These values represent our best-validated observations during what are recognized within the ionospheric community as the most extreme geomagnetic storms during and following the most recent solar maximum.

The most time-consuming aspect of ionospheric anomaly data analysis is manual review of the apparent anomalies output by the

automated-search software. In the majority of cases, it was evident to human eyes that receiver or postprocessing errors created an apparent ionospheric gradient that was not real, and these observations were set aside. However, a significant number of events that could not be discounted remained and were subjected to more detailed analysis by team consensus.

As a result of this work, we have validated low-elevation spatial gradients in the ionospheric delay at L1 as high as 360 and 413 mm/km at high elevation. These observations were made with CORS network stations in northern Ohio during the 20 Nov. 2003 ionospheric storm. Station redundancy rules out the possibility of these gradients being generated by faulty receivers or significant errors in receiver bias estimation. Simultaneous observations on other satellites at similar elevations were also unusually high. Therefore, we conclude that the largest gradients observed here were not due to nonionospheric causes.

The impact of these gradients on WAAS precision approach integrity is negligible due to the implementation of the WAAS extreme storm detector (however WAAS precision approach availability is dramatically affected when severe storms occur). Mitigating the safety threats posed by ionospheric storms to users of LAAS is achieved by disallowing specific user satellite geometries during precision approach, at the cost of somewhat reducing LAAS CAT 1 availability.

Acknowledgments

The authors thank the FAA LAAS Program Office for their support in the completion of this effort. We would also like to thank specific individuals who helped us in this work, including Todd Walter, Juan Blanch, and Shankar Ramakrishnan at Stanford, John Warburton and Tom Dehel of the Federal Aviation Administration William J. Hughes Technical Center, and Attila Komjathy of the NASA Jet Propulsion Laboratory.

References

[1] Enge, P., "Local Area Augmentation of GPS for the Precision Approach of Aircraft," *Proceedings of the IEEE*, Vol. 87, No. 1, Jan. 1999, pp. 111–132. doi:10.1109/5.736345

[2] Enge, P., Walter, T., Pullen, S., Kee, C., Chao, Y. C., and Tsai, Y. J., "Wide Area Augmentation of the Global Positioning System," *Proceedings of the IEEE*, Vol. 84, No. 8, Aug. 1996, pp. 1063–1088. doi:10.1109/5.533954

[3] Misra, P., and Enge, P., *Global Positioning System: Signals, Measurement, and Performance*, 2nd ed., Ganga–Jamuna, Lincoln, MA, 2006.

[4] Tascione, T. F., *Introduction to the Space Environment*, Krieger, Malabar, FL, 1994.

[5] Klobuchar, J., "Ionospheric Effects on GPS," *Global Positioning System: Theory and Applications*, edited by B. W. Parkinson and J. J. Spilker, Vol. 1, Progress in Astronautics and Aeronautics, AIAA, Washington, DC, 1996, pp. 485–515.

[6] Datta-Barua, S., Mannucci, A. J., Walter, T., and Enge, P., "Altitudinal Variation of Midlatitude Localized TEC Enhancement from Ground- and Space-Based Measurements," *Space Weather*, Vol. 6, No. S10D06, 2008. doi:10.1029/2008SW000396

[7] Roble, R. G., and Ridley, E. C., "Thermosphere–Ionosphere–Mesosphere Electrodynamics General Circulation Model (TIME-GCM): Equinox Solar Cycle Minimum Simulations (30–500 km)," *Geophysical Research Letters*, Vol. 21, No. 6, 1994, pp. 417–420. doi:10.1029/93GL03391

[8] Crowley, G., et al., "Global Thermosphere–Ionosphere Response to Onset of 20 November 2003 Magnetic Storm," *Journal of Geophysical Research*, Vol. 111, No. A10S18, 2006. doi:10.1029/2005JA011518

[9] Huba, J. D., Joyce, G., and Fedder, J. A., "Sami2 is Another Model of the Ionosphere (SAMI2): A New Low-Latitude Ionosphere Model," *Journal of Geophysical Research*, Vol. 105, No. A10, 2000, pp. 23035–23053. doi:10.1029/2000JA000035

[10] Bilitza, D., "International Reference Ionosphere 2000," *Radio Science*, Vol. 36, No. 2, March–April 2001, pp. 261–275. doi:10.1029/2000RS002432

[11] Pi, X., Wang, C., Hajj, G. A., Rosen, G., Wilson, B. D., and Bailey, G. J., "Estimation of ExB Drift Using a Global Assimilative Ionospheric Model: An Observation System Simulation Experiment," *Journal of Geophysical Research*, Vol. 108(A2), No. 1075, 2003. doi:10.1029/2001JA009235

[12] Schunk, R., et al., "Global Assimilation of Ionospheric Measurements (GAIM)," *Radio Science*, Vol. 39, No. RS1S02, 2004. doi:10.1029/2002RS002794

[13] Bust, G. S., et al., "Four-Dimensional GPS Imaging of Space Weather Storms," *Space Weather*, Vol. 5, No. S02003, 2007. doi:10.1029/2006SW000237

[14] Klobuchar, J. A., Doherty, P. H., and El-Arini, M. B., "Potential Ionospheric Limitations to Wide-Area Differential GPS," *Proceedings of the 16th International Technical Meeting of the Satellite Division of The Institute Of Navigation (ION GPS 1993)*, Salt Lake City, UT, 1993, pp. 1245–1254.

[15] Klobuchar, J. A., and Kunches, J., "Eye on the Ionosphere: The Spatial Variability of Ionospheric Range Delay," *GPS Solutions*, Vol. 3, No. 3, 2000, pp. 70–74. doi:10.1007/PL00012808

[16] Walter, T., et al., "Robust Detection of Ionospheric Irregularities," *Proceedings of ION GPS 2000*, http://waas.stanford.edu/~wwu/papers/gps/PDF/toddion00.pdf, Salt Lake City, UT, 2000, pp. 209–218.

[17] Christie, J. R. I., Ko, P.-Y., Hansen, A., Dai, D., Pullen, S., Pervan, B., and Parkinson, B., "The Effects of Local Ionospheric Decorrelation on LAAS: Theory and Experimental Results," *Proceedings of the Institute of Navigation National Technical Meeting*, 1999, pp. 769–777.

[18] "Minimum Operational Performance Standards for GPS Local Area Augmentation System Airborne Equipment," Radio Technical Commission for Aeronautics, Washington, D.C., Publ. DO-253C, 2008.

[19] Lee, J., Pullen, S., Datta-Barua, S., and Enge, P., "Assessment of Nominal Ionosphere Spatial Decorrelation for GPS-Based Aircraft Landing Systems," *Journal of Aircraft*, Vol. 44, No. 5, 2007, pp. 1662–1669. doi:10.2514/1.28199

[20] Datta-Barua, S., Walter, T., Pullen, S., Luo, M., Blanch, J., and Enge, P., "Using WAAS Ionospheric Data to Estimate LAAS Short Baseline Gradients," *Proceedings of the Institute of Navigation National Technical Meeting*, 2002, pp. 523–530.

[21] Luo, M., Pullen, S., Akos, D., Xie, G., Datta-Barua, S., Walter, T., and Enge, P., "Assessment of Ionospheric Impact on LAAS Using WAAS Supertruth Data," *Proceedings of the ION 58th Annual Meeting and CIGTF 21st Guidance Test Symposium*, 2002, pp. 175–186.

[22] Ene, A., Qiu, D., Luo, M., Pullen, S., and Enge, P., "A Comprehensive Ionosphere Storm Data Analysis Method to Support LAAS Threat Model Development," *Proceedings of the Institute of Navigation National Technical Meeting*, 2005, pp. 110–130.

[23] Ramakrishnan, S., Lee, J., Pullen, S., and Enge, P., "Targeted Ephemeris Decorrelation Parameter Inflation for Improved LAAS Availability During Severe Ionosphere Anomalies," *Proceedings of the 2008 National Technical Meeting of the Institute of Navigation*, pp. 354–366.

[24] Komjathy, A., L. Sparks, and A. J. Mannucci, "Generating High Precision Ionospheric Ground-Truth Measurements," U.S. Patent No. 7,289,061 B2, filed 30 Oct. 2007.

[25] Datta-Barua, S., "Ionospheric Threats to the Integrity of Airborne GPS Users," Ph.D. Dissertation, Stanford Univ., Palo Alto, CA, 2008.

[26] Luo, M., Pullen, S., Dennis, J., Konno, H., Xie, G., Walter, T., Enge, P., Datta-Barua, S., and Dehel, T., "LAAS Ionosphere Spatial Gradient Threat Model and Impact of LGF and Airborne Monitoring," *Proceedings of the 16th International Technical Meeting of the Satellite Division of the Institute of Navigation ION GPS/GNSS*, 2003, pp. 2255–2274.

[27] Luo, M., Pullen, S., Walter, T., and Enge, P., "Ionosphere Spatial Gradient Threat for LAAS: Mitigation and Tolerable Threat Space," *Proceedings of the 2004 National Technical Meeting of the Institute of Navigation*, pp. 490–501.

[28] National Geodetic Survey CORS Team, "CORS: Continuously Operating Reference Stations," http://www.ngs.noaa.gov/CORS/ [retrieved 6 Jan. 2009].

[29] National Geophysical Data Center, "Space Physics Interactive Data Resource," 2005, http:/spidr.ngdc.noaa.gov/spidr/ [retrieved 1 March 2005].

[30] Sugiura, M., and Kamei, T., "Equatorial Dst Index 1957–1986," *International Association of Geomagnetism and Aeronomy*, Vol. 40, 1991, pp. 7–14.

[31] Menvielle, M., and Berthelier, A., "The K-Derived Planetary Indices: Description and Availability," *Reviews of Geophysics*, Vol. 29, No. 3,

1991, pp. 415–432.
doi:10.1029/91RG00994

[32] Menvielle, M., and Berthelier, A., Correction to "The K-Derived Planetary Indices: Description and Availability," *Reviews of Geophysics*, Vol. 30, No. 1, 1992, p. 91.
doi:10.1029/92RG00461

[33] Poppe, B. B., "New Scales Help Public, Technicians Understand Space Weather," *Transactions of the American Geophysical Union*, Vol. 81, No. 29, 18 July 2000, pp. 322, 328,
doi:10.1029/00EO00247

[34] Komjathy, A., "Automated Daily Processing of more than 1000 Ground-Based GPS Receivers for Studying Intense Ionospheric Storms," *Radio Science*, Vol. 40, 2005, pp. RS6006.
doi:10.1029/2005RS003279

[35] Datta-Barua, S., "Ionosphere Threats to Space-Based Augmentation System Development," *Proceedings of the 17th International Technical Meeting of the Satellite Division of the Institute of Navigation ION GNSS 2004*, 2004, pp. 1308–1317.

[36] Simili, D. V., and Pervan, B., "Code-Carrier Divergence Monitoring for the GPS Local Area Augmentation System," *Proceedings of IEEE/ION PLANS 2006*, San Diego, CA, 25–27 April 2006, pp. 483–493.

[37] Luo, M., Pullen, S., Datta-Barua, S., Zhang, G., Walter, T., and Enge, P., "LAAS Study of Slow-Moving Ionosphere Anomalies and Their Potential Impact," *Proceedings of the 18th International Technical Meeting of the Satellite Division of the Institute of Navigation ION GNSS 2005*, 2005, pp. 2337–2349.

[38] Lee, J., Luo, M., Pullen, S., Park, Y. S., Enge, P., and Brenner, M., "Position-Domain Geometry Screening to Maximize LAAS Availability in the Presence of Ionosphere Anomalies," *Proceedings of the 19th International Technical Meeting of the Satellite Division of the Institute of Navigation ION GNSS 2006*, pp. 393–408.

[39] Warburton, J., "FAA HMI Analysis and Integrity Risk Compliance Arguments (IRCAs)," International GBAS Working Group (I-GWG) 8 Meeting, Agenda Item 6.2, Palermo, Italy, 3–6 March 2009.